

Supporting information

Ca²⁺ and Ag⁺ orient low-molecular weight amphiphile self-assembly into “nano-fishnet” fibrillar hydrogels with unusual β -sheet-like raft domains

Alexandre Poirier,^a Patrick Le Griel,^a Ingo Hoffmann,^b Javier Perez,^c Petra Pernot,^d Jérôme Fresnais,^e Niki Baccile^{a,*}

^a Sorbonne Université, Centre National de la Recherche Scientifique, Laboratoire de Chimie de la Matière Condensée de Paris, LCMCP, F-75005 Paris, France

^b Institut Laue-Langevin, 38042 Grenoble, France

^c Synchrotron Soleil, L'Orme des Merisiers, Saint-Aubin, BP48, 91192 Gif-sur-Yvette Cedex, France

^d ESRF – The European Synchrotron, CS40220, 38043 Grenoble, France

^e Sorbonne Université, CNRS, Laboratoire de Physico-chimie des Électrolytes et Nanosystèmes Interfaciaux, PHENIX - UMR 8234, F-75252, Paris Cedex 05, France

* Corresponding author:

Dr. Niki Baccile

E-mail address: niki.baccile@sorbonne-universite.fr

Phone: +33 1 44 27 56 77

Experimental

Neutron spin echo (NSE). Neutron Spin-Echo (NSE)¹ measurements have been performed at the instrument IN15² at the Institut Laue-Langevin (ILL) in Grenoble (France). Four different wavelengths (λ) have been used, namely 13.5, 12, 10 and 8 Å allowing to reach maximum Fourier times t of 477, 335, 194 and 99 ns, respectively and covering a q -range from 0.03 to 0.14 Å⁻¹, where $q = \frac{4\pi}{\lambda} \sin(\frac{\theta}{2})$ is the modulus of the scattering vector, with scattering angle θ . The data were corrected for resolution effects using graphite and the scattering from the aqueous background was subtracted. Experiments were performed in a fully deuterated (D₂O) medium.

To analyze the data, the Zilman-Granek model³ was applied. Starting from a Helfrich bending Hamiltonian,⁴ it predicts a stretched exponential shape of the intermediate scattering function $S(q, t)$ (Eq. 1) with a stretch exponential $\beta = 2/3$, $I(q, t)$ being the spin echo intensity at a given value of q and time, t

$$\frac{I(q,t)}{I(q,0)} = S(q, t) = e^{-(\Gamma_{ZG}t)^\beta} \quad \text{Eq. S1}$$

where

$$\Gamma_{ZG} = \alpha\gamma \left(\frac{k_b T}{\kappa}\right)^{\frac{1}{2}} \left(\frac{k_b T}{\eta}\right) q^3 \quad \text{Eq. S2}$$

from which, the scaled bending rigidity, κ , is

$$\frac{\kappa}{k_b T} = \left(\frac{\alpha\gamma}{\eta} (k_b T)^{\frac{1}{2}} \frac{q^3}{\Gamma_{ZG}}\right)^2 \quad \text{Eq. S3}$$

where α is a prefactor, $\gamma \approx 1$ for $\frac{k_b T}{\kappa} \ll 1$, η is the solvent viscosity (generally $\eta(\text{D}_2\text{O}) = 1.1 \cdot 10^{-3}$ Pa.s at 25°C), k_b is the Boltzmann constant, T is the temperature in Kelvin.

Small angle X-ray scattering (SAXS). SAXS experiments have been performed on various beamlines and synchrotron facilities. The environments as well as the samples associated to each session are presented below.

Capillary SAXS. SAXS experiments are performed using hydrogel samples prepared at room temperature and analyzed into 1.5 mm quartz capillaries on the Swing beamline (proposal N° 20201747) at Soleil Synchrotron (Saint-Aubin, France) and on the BM29 beamline at the ESRF Synchrotron (Grenoble, France). Samples are manually injected into the capillary using a 1.0

mL syringe. The Swing beamline is used with an energy of $E = 12$ keV and a fixed sample-to-detector (Eiger 4M - Dectris) distance of 2.005 m. An additional run has also been performed on the SWING beamline (proposal Number: BAG 20201118), with $E = 12$ keV and two sample-to-detector distances, 6.60 m and 0.50 m.

The BM29 beamline (Proposal N° MX 2311) is used with an energy of $E = 12.5$ KeV and a sample-to-detector distance of 2.83 m. q is the wave vector, with $q = 4\pi/\lambda \sin(\theta)$, 2θ corresponding to the scattering angle and λ the wavelength. The q -range is calibrated between $\sim 0.05 < q / \text{nm}^{-1} < \sim 5$, using the standard silver behenate calibrant ($d_{(001)} = 58.38 \text{ \AA}$); raw data obtained on the 2D detector are integrated azimuthally using the in-house software provided at the beamline and thus to obtain the typical scattered intensity $I(q)$ profile. Absolute intensity units are determined by measuring the scattering signal of water ($I(q=0) = 0.0163 \text{ cm}^{-1}$).

Figure	Sample	Experiment	Beamline	Synchrotron	Proposal N°
3a, 3b	{Ca ²⁺ }G-C18:1, no shear	Capillary SAXS	SWING	Soleil	BAG 20201118
3a, 3b	{Ca ²⁺ }G-C18:1 shear {Ca ²⁺ }G-C18:1, no shear G-C18:1	Capillary SAXS	BM29	ESRF	MX 2311
3a	{Ag ⁺ }G-C18:1 shear	Capillary SAXS	SWING	Soleil	20201747
S 1, S 4a,b	All	Capillary SAXS	BM29	ESRF	MX 2311
S 5	pH 8	Capillary SAXS	BM29	ESRF	MX 2311

Cryogenic-transmission electron microscopy (Cryo-TEM). Pictures are recorded on an FEI Tecnai 120 twin microscope operating at 120 kV with an Orius 1000 CCD numeric camera. The sample holder is a Gatan Cryo holder (Gatan 626DH, Gatan). Digital Micrograph software is used for image acquisition. Cryo-fixation is done with low dose on a homemade cryo-fixation device. The solutions are deposited on a glow-discharged holey carbon coated TEM nickel grid (Quantifoil R2/2, Germany). Excess solution is removed and the grid is immediately plunged into liquid ethane at -180°C before transferring them into liquid nitrogen. All grids are kept at liquid nitrogen temperature throughout all experimentation. Cryo-TEM images are treated and analyzed using Fiji software, available free of charge at the developer's web site.⁵

Isothermal titration calorimetry (ITC). ITC experiments are performed using a nano-ITC from TA Instruments. A water solution is prepared at pH 8 and used as solvent by G-C18:1. Note that a classical phosphate buffer solution could not be used due to a side reaction with

calcium. All solutions are degassed during 20 min under vacuum (400 mmHg). The titration experiments between calcium chloride, or silver nitrate, and G-C18:1 employ a solution at pH 8 of calcium chloride as titrant at concentration of 80 et 50 mM. The titrated solution corresponds to 20 mM of G-C18:1 at pH in water, freshly prepared before the experiment to prevent precipitation of calcium hydroxide. Experiments are run at 23°C, 25 injections of 10 μ L of titrant each every 300 s. To take account of dilution effects, all titration experiments are followed by the same experiment without G-C18:1 in water at pH 8, which is used as a control, subtracted to the original titration measurement. The mixing rotation of the syringe was established to 200 rpm.

Data are fitted using a multi-site model using Nano-data analysis software (TA Instruments) in order to determine the thermodynamic as well as the reaction parameters of the interaction between Ca^{2+} and G-C18:1. From the enthalpy (ΔH) and the binding constant (K_a) of the reaction, the entropy (ΔS) and the Gibbs free energy (ΔG) of reaction were calculated using the equation $\Delta G = \Delta H - T\Delta S = -RT \cdot \ln(K_a)$. For the titration of Ag^+ and G-C18-1, an independent model is used, as a single reaction is observed.

Solid-state nuclear magnetic resonance (ssNMR). ^{13}C solid-state NMR experiments were carried out on an Avance III HD Bruker 7.05 T ($\nu_{\text{H}} = 300$ MHz) spectrometer and a 4 mm magic angle spinning (MAS) probe. The ^{13}C NMR spectra were obtained by $^1\text{H} \rightarrow ^{13}\text{C}$ cross-polarization (CP) under magic angle spinning (MAS). $\nu_{\text{MAS}} = 10$ kHz, number of transients, NS = 1024; time domain size, TD = 2 k; pulse length, $p(^1\text{H}) = 7.00$ μs , $p(^{13}\text{C}) = 3.62$ μs , relaxation delay, D = 3 s; CP is performed under ramped (square) conditions with contact time during CP, t_c being indicated in the main text.

Table S 1 – Literature survey based on the scattering (SAXS or SANS) data reported in each cited article. Articles cited under *SAFiN with disordered fibers* report a typical scattering profile of the fiber alone, with or without a structure peak. Articles cited under *SAFiN with suprafibrillar assembly* report scattering profiles where the fiber’s form factor is superimposed with the structure factor associated to the 3D organization of the fibers. Articles cited under *β -sheet-like gel (“nano-fishnet”)* report those hydrogels characterized by entanglement and β -sheet or β -sheet-like structure.

SAFiN with disordered fibers	
Not gelled	6–9
Gels	10,11,20–22,12–19
SAFiN with suprafibrillar assembly	
Hexagonal bundles/Columnar hexagonal	23–28
Raft-like/lamellar (solution, not gelled)	29,30
β-sheet-like gel (“nano-fishnet”)	
Biopolymers (fibroin, actin)	31–38
SAFiN	This work

Table S 2 - Table of correlation peaks related to SAXS data presented in Figure 3 in the main text. a) Correlation peaks of 3 wt% G-C18:1 at basic pH and $[Ca^{2+}]/[G-C18:1]= 0.61$. b) Correlation peaks of 3 wt% G-C18:1 at basic pH with $[Ag^+]/[G-C18:1]= 1.0$.

$[Ca^{2+}]/[G-C18:1]= 0.61$, $C_{G-C18:1}= 3$ wt%

Sheared gel			Static gel		
Peak	position / nm^{-1}	ratio	Peak	position / nm^{-1}	ratio
q_{f1}	2.41	-	1	0.62	1
q_{f2}	3.02	1.25	2	1.35	2.2
q_{f3}	4.71	$\sqrt{2}$	3	1.81	2.9
			4	2.48	4.0
			5	3.18	5.1
			6	3.73	6.0
			7	4.49	7.2
			8	4.88	7.9
			9	5.68	9.2

$[Ag^+]/[G-C18:1]= 1$, $C_{G-C18:1}= 3$ wt%

Peak	position / nm^{-1}	ratio
1	1.18	1
2	2.40	2.03
3	3.52	2.98
4	4.74	4.02

a)

b)

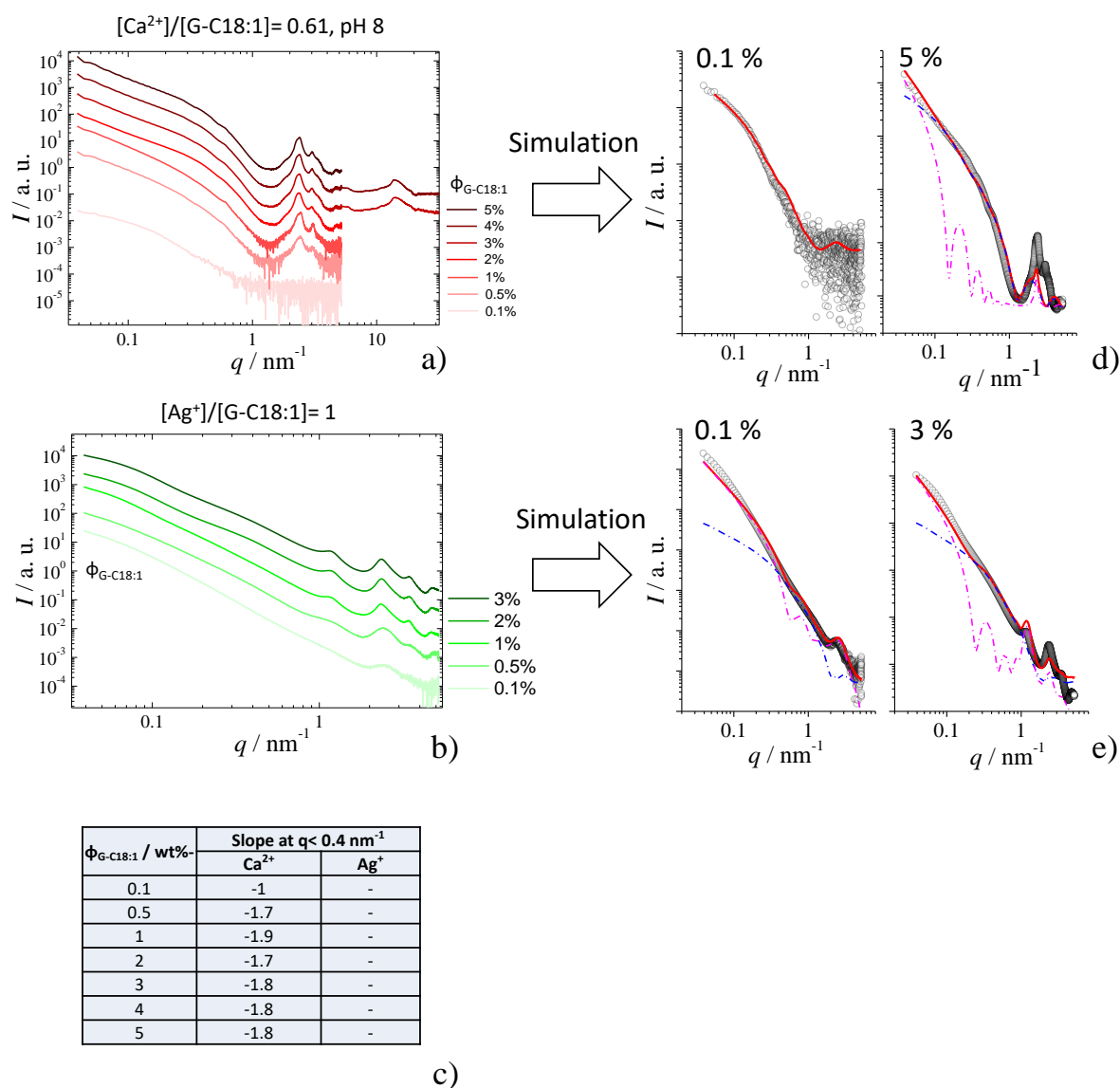


Figure S 1 – SAXS profiles recorded as a function of G-C18:1 concentration at basic pH for a) $\{Ca^{2+}\}G-C18:1$ and b) $\{Ag^{+}\}G-C18:1$ gels. Table in c) illustrates the $\log(I)-\log(q)$ dependency (slope) for the Ca^{2+} system. The slopes for the Ag^{+} cannot be reasonably estimated due to the overlap of two scattering signals below about 0.2 nm^{-1} . d-e) Simulated SAXS curves extracted from the experiments in a-b): $\{Ca^{2+}\}G-C18:1$ (0.1 wt%, 5 wt%) and $\{Ag^{+}\}G-C18:1$ (0.1 wt%, 3 wt%). Magenta segmented curves employ model *M1*; blue segmented curves employ model *M2*; red solid curve employ the sum of *M1* and *M2*. Simulation was performed with form factor models available in SasView 3.1.2 software. The full list of parameters and model description is given in Table S 3 and Page S 8 to Page S 10 in the Supporting Information.

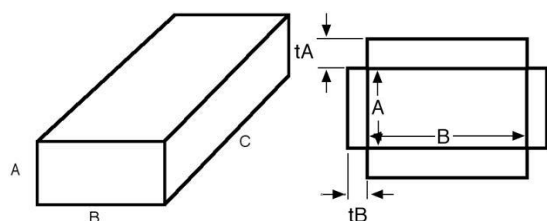
Table S 3 – Set of the numerical parameters used for the form factor models employed to simulate SAXS curves of {Ca²⁺}G-C18:1 (0.1 wt%, 5 wt%) and {Ag⁺}G-C18:1 (0.1 wt%, 3 wt%). Simulations are shown in Figure S 1d,e: magenta segmented curves employ model *M1*; blue segmented curves employ model *M2*; red solid curve employ the sum of *M1* and *M2*.

***M1* (core-shell parallelepiped model) and *M2* (lamellar paracrystal model) are shortly described below.**

{Ca²⁺}G-C18:1	
[Ca ²⁺]/[G-C18:1]= 0.61, pH 8	
0.1 wt%	5 wt%
<i>M1</i> _background = 0.00003 1/cm <i>M1</i> _longC = 100 nm <i>M1</i> _midB = 30 nm <i>M1</i> _rimA = 1 nm <i>M1</i> _rimB = 0 nm <i>M1</i> _rimC = 0 nm <i>M1</i> _scale = 0.05 <i>M1</i> _shortA = 2.6 nm <i>M1</i> _sld_pcore = 8.0e-04 1/nm ² <i>M1</i> _sld_rimA = 1.6e-03 1/nm ² <i>M1</i> _sld_rimB = - <i>M1</i> _sld_rimC = - <i>M1</i> _sld_solv = 9.4e-04 1/nm ²	<i>M1</i> _background = 0.3 1/cm <i>M1</i> _longC = 100 nm <i>M1</i> _midB = 25 nm <i>M1</i> _rimA = 1.45 nm <i>M1</i> _rimB = 0 nm <i>M1</i> _rimC = 0 nm <i>M1</i> _scale = 10000 <i>M1</i> _shortA = 3.3 nm <i>M1</i> _sld_pcore = 8.0e-04 1/nm ² <i>M1</i> _sld_rimA = 1.8e-03 1/nm ² <i>M1</i> _sld_rimB = - <i>M1</i> _sld_rimC = - <i>M1</i> _sld_solv = 9.4e-06 1/nm ² <i>M2</i> _background = 0.3 1/cm <i>M2</i> _Nlayers = 15 <i>M2</i> _pd_spacing = 0.1 <i>M2</i> _scale = 500 <i>M2</i> _sld_layer = 11.5e-04 1/nm ² <i>M2</i> _sld_solvent = 9.4e-04 1/nm ² <i>M2</i> _spacing = 2.7 nm <i>M2</i> _thickness = 0.5 nm scale_factor = 1
{Ag⁺}G-C18:1	
[Ag ⁺]/[G-C18:1]= 1, pH 8	
0.1 wt%	3 wt%
<i>M1</i> _background = 0.00005 1/cm <i>M1</i> _longC = 100 nm <i>M1</i> _midB = 10 nm <i>M1</i> _rimA = 1 nm <i>M1</i> _rimB = 0 nm <i>M1</i> _rimC = 0 nm <i>M1</i> _scale = 0.1 <i>M1</i> _shortA = 2.8 nm <i>M1</i> _sld_pcore = 3e-04 1/nm ² <i>M1</i> _sld_rimA = 11e-04 1/nm ² <i>M1</i> _sld_rimB = - <i>M1</i> _sld_rimC = - <i>M1</i> _sld_solv = 9.4e-04 1/nm ² <i>M2</i> _background = 0 1/cm <i>M2</i> _Nlayers = 5 <i>M2</i> _pd_spacing = 0.25 <i>M2</i> _scale = 2.9 <i>M2</i> _sld_layer = 11e-04 1/nm ² <i>M2</i> _sld_solvent = 9.4e-04 1/nm ² <i>M2</i> _spacing = 2.2 nm <i>M2</i> _thickness = 1 nm scale_factor = 1	<i>M1</i> _background = 0.4 1/cm <i>M1</i> _longC = 100 nm <i>M1</i> _midB = 10 nm <i>M1</i> _rimA = 1 nm <i>M1</i> _rimB = 0 nm <i>M1</i> _rimC = 0 nm <i>M1</i> _scale = 310 <i>M1</i> _shortA = 2.8 nm <i>M1</i> _sld_pcore = 4e-06 1/nm ² <i>M1</i> _sld_rimA = 20e-06 1/nm ² <i>M1</i> _sld_rimB = - <i>M1</i> _sld_rimC = - <i>M1</i> _sld_solv = 9.4e-04 1/nm ² <i>M2</i> _background = 0.008 1/cm <i>M2</i> _Nlayers = 5 <i>M2</i> _pd_spacing = 0.13 <i>M2</i> _scale = 1000 <i>M2</i> _sld_layer = 11.6e-04 1/nm ² <i>M2</i> _sld_solvent = 9.4e-04 1/nm ² <i>M2</i> _spacing = 5.1 nm <i>M2</i> _thickness = 0.5 nm scale_factor = 1

Simulations were performed with form factor models available in the software SasView 3.1.2.³⁹ Full model description can be found in the documentation of SasView,³⁹ while a short description follows.

* *Model, M1, CSParallelepipedModel*: Calculates the form factor for a rectangular solid with a core-shell structure. The thickness and the scattering length density of the shell or “rim” can be different on all three (pairs) of faces.



* *Model, M2, LamellarPCrystalModel*: This model calculates the scattering from a stack of repeating lamellar structures. The stacks of lamellae (infinite in lateral dimension) are treated as a paracrystal to account for the repeating spacing.

The choice of *M1* and *M2*, as well as the parameters listed in Table S 3, was based on the knowledge of the system, estimated by the chemical structure of G-C18:1 and cryo-TEM data presented in the main text. From cryo-TEM, one observes fibers with a flat cross-section. On the other hand, previous modelling of SAXS profiles characterizing the self-assembly of G-C18:1 required the use of a core-shell model.⁴⁰ For this reason, we selected a core-shell parallelepiped form factor model (*M1*). *M1* reveals to be particularly efficient in modelling the SAXS profile of {Ca²⁺}G-C18:1 under diluted conditions at 0.1 wt% (Figure S 1d), where fibers do not interact with each other. On the other hand, all other samples could only be modelled with a second contribution, namely a lamellar paracrystal (*M2*). Employing *M2* is justified by the cryo-TEM images in the main text, which show the assembly of the fibers into lamellar rafts. Lamellar rafts contribute both to the low-q scattering as a flat morphology but also to the lamellar structure factor at mid-q/high-q. Unfortunately, SasView does not provide any valuable structure factor allowing simulation of the diffraction peaks found in {Ca²⁺}G-C18:1 at 3 wt%.

The list of the parameters given in Table S 3 is given hereafter and discussed below.

Form factor for a rectangular Shell. Below are the Parameters.

scale: scale factor

shortA: length of short edge [A]

midB: length of another short edge [A]

longC: length of long edge of the parallelepiped [A]

rimA: length of short edge [A]

rimB: length of another short edge [A]

rimC: length of long edge of the parallelepiped [A]

sld_rimA: sld of rimA [1/A²]

sld_rimB: sld of rimB [1/A²]

sld_rimC: sld of rimC [1/A²]

sld_core: Pipe_sld [1/A²]

sld_solv: solvent_sld [1/A²]

background: incoherent Background [1/cm]

[Lamellar ParaCrystal Model] Parameter Definitions: scale = scale factor,
background = incoherent background
thickness = lamellar thickness,
sld_layer = layer scattering length density,
sld_solvent = solvent scattering length density.
Nlayers = no. of lamellar layers
spacing = spacing between layers
pd_spacing = polydispersity of spacing

Parameters were accurately selected to keep the physics of the model as close as possible to the experimental data. For instance, the value of $9.4 \cdot 10^{-4} \text{ 1/nm}^2$ for the sld (scattering length density) of the solvent reflects the value for water. The sld of the core, classically in the order of $8 \cdot 10^{-4} \text{ 1/nm}^2$ for a hydrocarbon, was tentatively modified only if necessary, and possibly reflecting the higher contrast between the core, the shell and the solvent. Some parameters did not have any influence, like the size of the rim B and rim C. These were set to zero. The length of the C axis is also not important, provided it is sufficiently long. The arbitrary value of 100 nm chosen here was satisfactory for the simulation. Other parameters were, on the contrary, critical and were adapted manually with extreme care. In *M1*, these are the B and A sides, the rim of A, the sld of the A-rim. In *M2*, these are the spacing, the polydispersity of the spacing, the number of layers and the thickness. The choice of the scale was always arbitrary.

Please note that the values given in Table S 3 are indicative of an order of magnitude and should not be taken as accurate. These were optimized manually for the purpose of the simulation but they are not the result of a numerical fitting process, which revealed to be too complex, due to the large number of critical free variables.

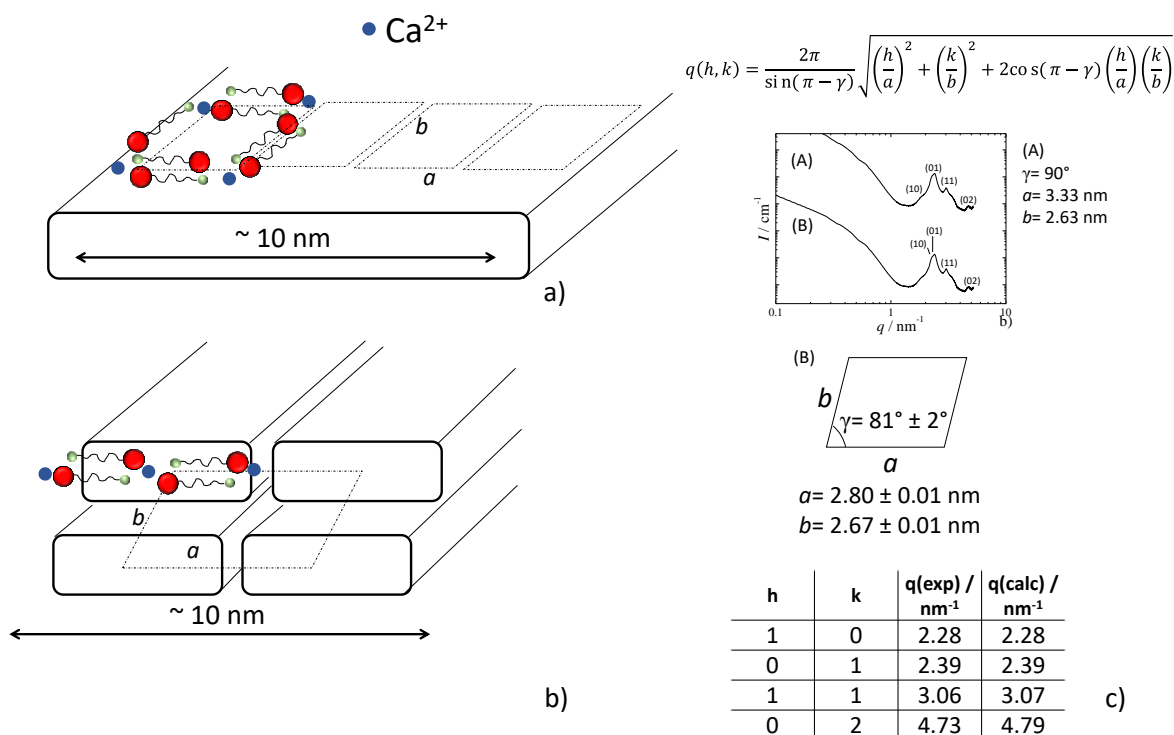
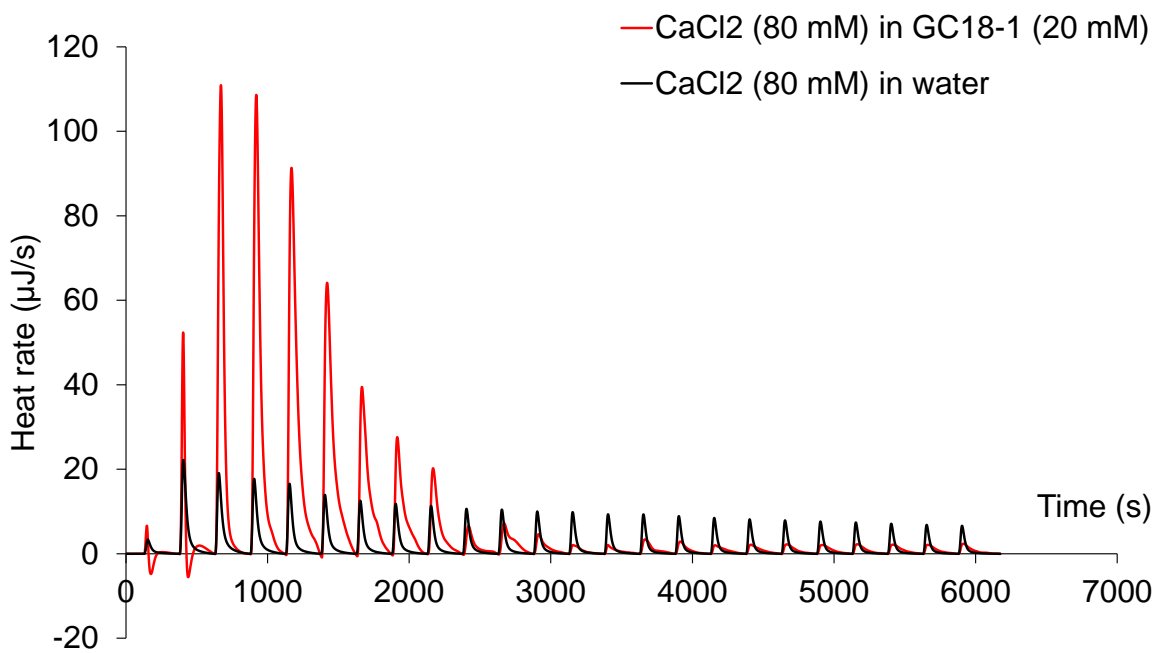
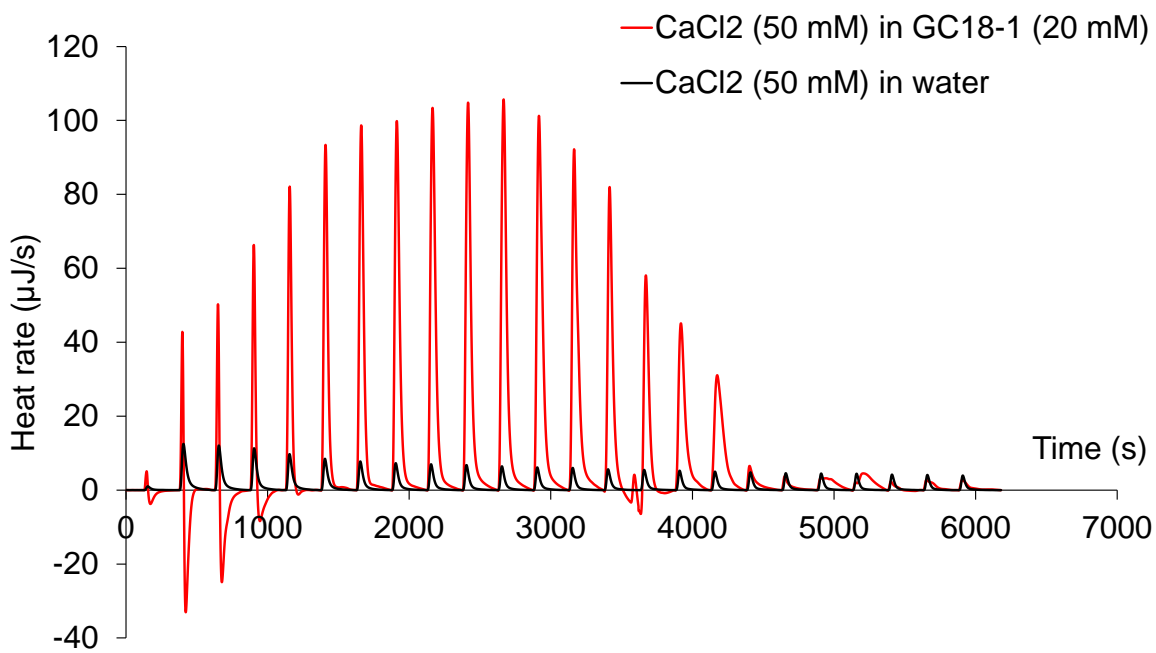


Figure S 2 –Possible arrangements of Ca²⁺ and G-C18:1 within an oblique lattice either a) within (according to ref. ^{41,42}) or b) orthogonal (ribbon phase^{43,44}) to the fiber’s longitudinal axis. c) (A) and (B) show the possible attributions of the Bragg peaks typically found in sheared {Ca²⁺}G-C18:1 samples.

Figure S 2 shows the tentative attribution of the peaks and evaluation of the fiber’s structure. First of all, one could pinpoint the main peaks at $q_1 = 2.41 \text{ nm}^{-1}$, $q_2 = 3.02 \text{ nm}^{-1}$ and $q_3 = 4.71 \text{ nm}^{-1}$, identifying a ratio of $q_2/q_1 = 1.25$ and $q_3/q_1 = 1.95 (\sim 2)$. Many similar SAFiN systems only show one main structural peak corresponding to an inter-lipid distance,^{9,45} or an hexagonal order ($1 : \sqrt{3} \equiv 1.73 : 2$) within the fiber (Table S 1). However, the peak positional ratio $q_2/q_1 = 1.25$ found here is quite atypical. If such ratio certainly excludes any lamellar and hexagonal arrangement, as well as all cubic phases due to the strong anisotropy of the fibers, two other possibilities exist. In the first one, one could suppose a ribbon mesophase with a rectangular, or oblique, 2D lattice orthogonal to the fiber’s longitudinal axis (Figure S 2b);^{43,44} in the second one, one could suppose a flat ribbon with a rectangular, or oblique, crystalline arrangement of the lipids within the fiber’s plane (Figure S 2a).^{41,42} The values of calculated wavevectors, $q(\text{calc})$, match well the experimental data, $q(\text{exp})$, as shown in Figure S 2b, when a 2D rectangular/oblique lattice with $(h,k) = 1,0; 0,1; 1,1; 0,2$ is employed. However, the rectangular lattice ($\gamma = 90^\circ$, hypothesis (A) in Figure S 2b) requires indexing the broad shoulder at 1.8 nm^{-1} as the $(1,0)$ plane. Although not impossible, this hypothesis seems to be inconsistent when

considering the peak width, much broader for (1,0) than for all other reflections. On the contrary, the use of an oblique lattice requires indexing of the multicomposite peak at about 2.40 nm^{-1} (hypothesis (B) in Figure S 2b). For this hypothesis, the broad shoulders at 1.8 nm^{-1} and 3.5 nm^{-1} could be attributed to the subjacent oscillation of the form factor. Possibly, one last hypothesis could leave room for interpreting the data as a combination of coexisting polymorphs with similar periods, as recently proposed for comparable glycolipid fibrillary hydrogels.^{46,47} Finally, a broad peak is observed at 13.9 nm^{-1} (Figure S 1a), corresponding to a d-spacing of 0.45 nm, compatible with an intra-alkyl chain distance, generally poorly affected by molecular packing.^{48,49} Although important, a detailed study of the crystal structure of SAFiN is a task *per se* and out of the scope of this work.



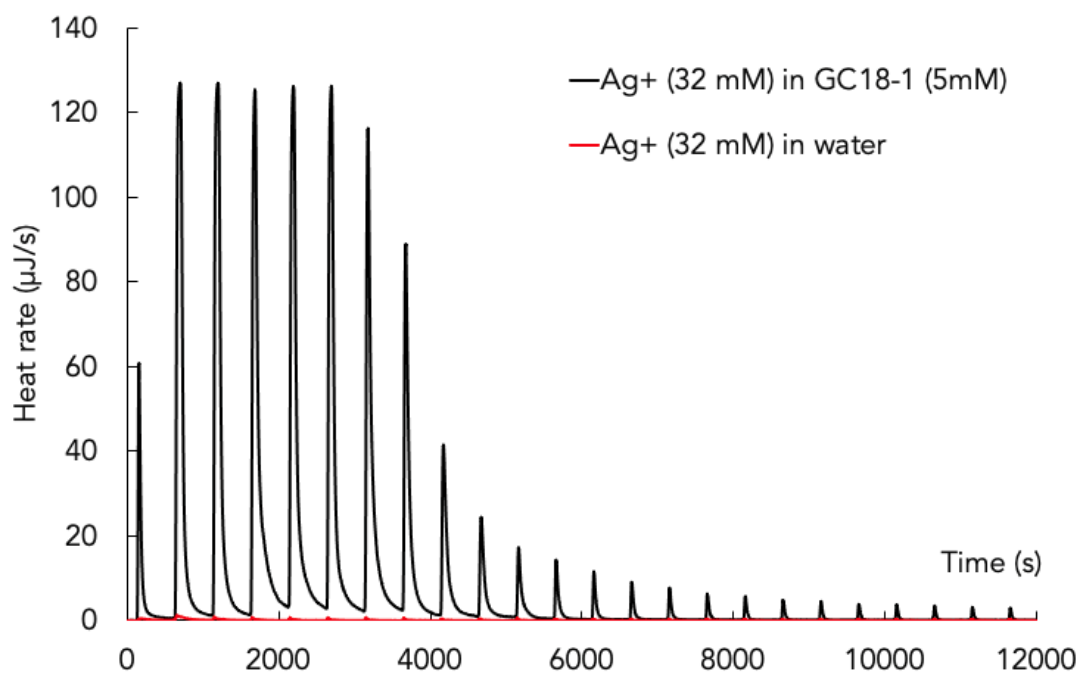


Figure S 3 – Calorimetric titrations (24 injections of 10 μL each) of a G-C18:1 solution (20 mM) with a solution of 50 mM of 80 mM CaCl_2 . Calorimetric titrations (24 injections of 10 μL each) of a G-C18:1 solution (5 mM) with a solution of 32 mM AgNO_3 .

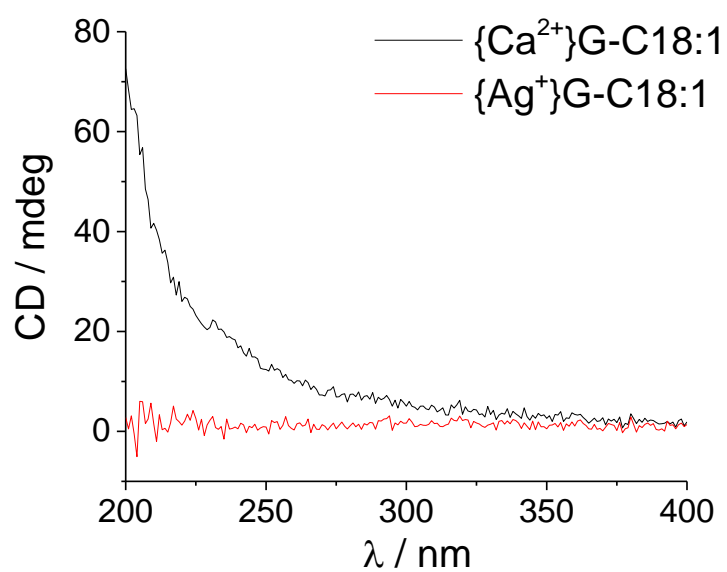


Figure S 4 – Circular dichroism spectra recorded on typical $\{Ag^{+}\}G-C8:1$ and $\{Ca^{2+}\}G-C18:1$ gels prepared at 3 wt% in water.

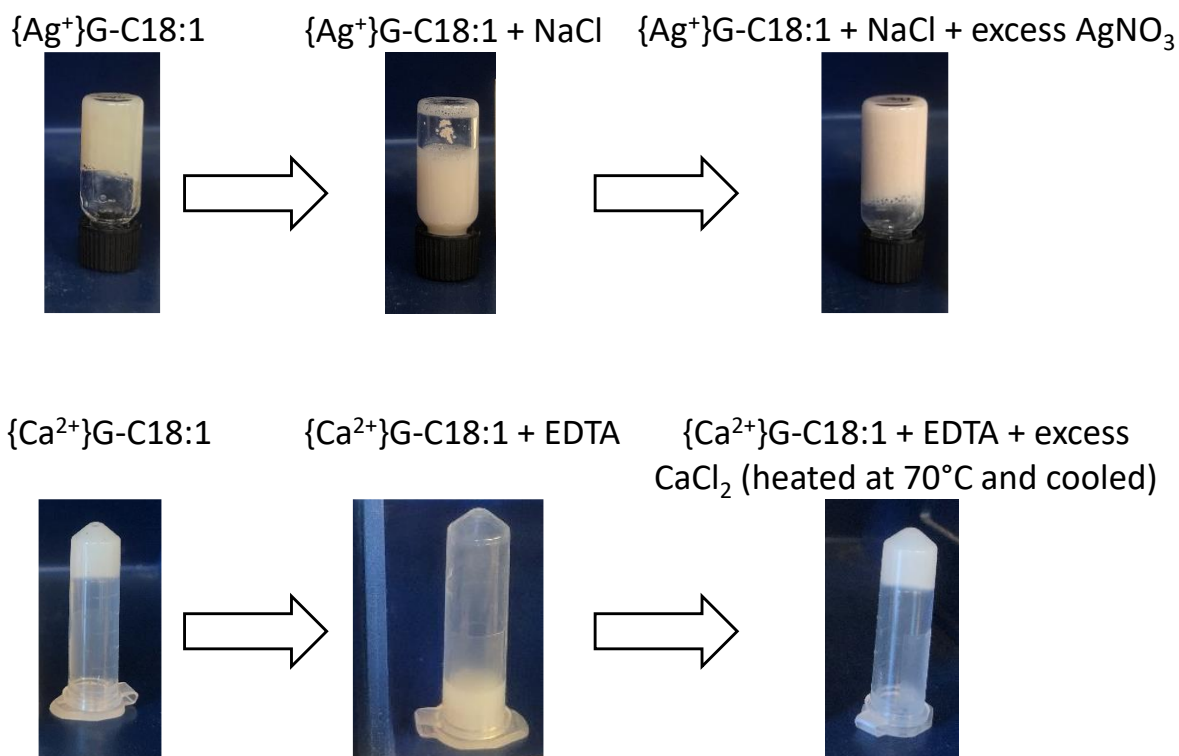


Figure S 5 – Stability and reversibility tests employing ethylenediaminetetraacetate (EDTA) and NaCl. EDTA complexes Ca^{2+} ions and it is employed with $\{Ca^{2+}\}G-C18:1$ gels, while NaCl precipitates silver ion as AgCl and it is used with $\{Ag^+\}G-C18:1$ gels (gel volume 1 mL). For $\{Ag^+\}G-C18:1$, we sequentially employ: $C_{G-C18:1} = 3 \text{ wt\%}$ at pH 10 with $[AgNO_3] = 65.2 \text{ mM} \rightarrow$ a gel forms. $[NaCl] = 65.2 \text{ mM}$ destabilizes the gel. $[AgNO_3] = 130.4 \text{ mM}$ are added and the gel forms again. For $\{Ca^{2+}\}G-C18:1$, we sequentially employ: $C_{G-C18:1} = 3 \text{ wt\%}$ at pH 10 with $[CaCl_2] = 40.0 \text{ mM} \rightarrow$ a gel forms (gel volume $500 \mu\text{L}$). $4 \mu\text{L}$ of a saturated EDTA solution destabilizes the gel into a liquid sol and reduces pH to 5.9. $[CaCl_2] = 80.0 \text{ mM}$ are added \rightarrow the solution is still liquid. $[NaOH] = 40 \text{ mM}$, pH raises from 6.7 to $\geq 10 \rightarrow$ the solution still liquid. Heating at $70^\circ C$ during 5 min and cooling at room temperature \rightarrow a gel forms.

References

1. Mezei, F. Neutron spin echo. in *Lecture Notes in Physics* (ed. Mezei, F.) 1–26 (Springer, 1980).
2. Farago, B. *et al.* The in15 upgrade. *Neutron News* **26**, 15 (2015).
3. Zilman, A. G. & Granek, R. Undulations and dynamic structure factor of membranes. *Phys. Rev. Lett.* **77**, 4788 (1996).
4. Helfrich, W. Elastic Properties of Lipid Bilayers - Theory and Possible Experiments. *Z. Naturforsch* **28**, 693–703 (1973).
5. Schindelin, J. *et al.* Fiji: an open-source platform for biological-image analysis. *Nat. Methods* **9**, 676–682 (2012).
6. Besenius, P. *et al.* Controlling the growth and shape of chiral supramolecular polymers in water. *Proc. Natl. Acad. Sci. U. S. A.* **107**, 17888–17893 (2010).
7. Adamcik, J. *et al.* Microtubule-Binding R3 Fragment from Tau Self-Assembles into Giant Multistranded Amyloid Ribbons. *Angew. Chemie - Int. Ed.* **55**, 618–622 (2016).
8. Pomerantz, W. C. *et al.* Nanofibers and lyotropic liquid crystals from a class of self-assembling β -peptides. *Angew. Chemie - Int. Ed.* **47**, 1241–1244 (2008).
9. Cui, H., Muraoka, T., Cheetham, A. G. & Stupp, S. I. Self-Assembly of Giant Peptide Nanobelts. *Nano Lett.* **9**, 945–951 (2009).
10. Calabrese, V. *et al.* Understanding heat driven gelation of anionic cellulose nanofibrils: Combining saturation transfer difference (STD) NMR, small angle X-ray scattering (SAXS) and rheology. *J. Colloid Interface Sci.* **535**, 205–213 (2019).
11. Cui, H., Cheetham, A. G., Pashuck, E. T. & Stupp, S. I. Amino acid sequence in constitutionally isomeric tetrapeptide amphiphiles dictates architecture of one-dimensional nanostructures. *J. Am. Chem. Soc.* **136**, 12461–12468 (2014).
12. Hule, R. A., Nagarkar, R. P., Hammouda, B., Schneider, J. P. & Pochan, D. J. Dependence of self-assembled peptide hydrogel network structure on local fibril nanostructure. *Macromolecules* **42**, 7137–7145 (2009).
13. Nagy-Smith, K. *et al.* Molecular, Local, and Network-Level Basis for the Enhanced Stiffness of Hydrogel Networks Formed from Coassembled Racemic Peptides: Predictions from Pauling and Corey. *ACS Cent. Sci.* **3**, 586–597 (2017).
14. Novelli, F. *et al.* Polymorphic Self-Organization of Lauroyl Peptide in Response to pH and Concentration. *Langmuir* **36**, 3941–3951 (2020).
15. Okesola, B. O. *et al.* Supramolecular Self-Assembly to Control Structural and Biological Properties of Multicomponent Hydrogels. *Chem. Mater.* **31**, 7883–7897 (2019).
16. Roberts, D., Rochas, C., Saiani, A. & Miller, A. F. Roberts Effect of Peptide and Guest Charge on the Structural, Mechanical.pdf. (2012).
17. Schmitt, J. *et al.* TEMPO-oxidised cellulose nanofibrils; Probing the mechanisms of gelation: Via small angle X-ray scattering. *Phys. Chem. Chem. Phys.* **20**, 16012–16020 (2018).
18. Yu, Z., Tantakitti, F., Palmer, L. C. & Stupp, S. I. Asymmetric Peptide Nanoribbons. *Nano Lett.* **16**, 6967–6974 (2016).
19. Zhang, S. *et al.* A self-assembly pathway to aligned monodomain gels. *Nat. Mater.* **9**, 594–601 (2010).
20. Draper, E. R. *et al.* Using Small-Angle Scattering and Contrast Matching to Understand Molecular Packing in Low Molecular Weight Gels. *Matter* **2**, 764–778 (2020).
21. Mallia, V. A. & Weiss, R. G. Structure-Property Comparison and Self-Assembly Studies of Molecular Gels Derived from (R)-12-Hydroxystearic Acid Derivatives as Low Molecular Mass Gelators. *ACS Symp. Ser.* **1296**, 227–243 (2018).
22. McAulay, K. *et al.* Isotopic Control over Self-Assembly in Supramolecular Gels. *Langmuir* **36**, 8626–8631 (2020).
23. Terech, P. & Maitra, U. Structural and rheological properties of aqueous viscoelastic solutions and gels of tripodal cholamide-based self-assembled supramolecules. *J. Phys. Chem. B* **112**, 13483–13492 (2008).
24. Stupp, S. I., Zha, R. H., Palmer, L. C., Cui, H. & Bitton, R. Self-assembly of biomolecular soft matter. *Faraday Discuss.* **166**, 9–30 (2013).
25. Wang, Y. *et al.* Polyamine-induced, chiral expression from liquid crystalline peptide nanofilaments to long-range ordered nanohelices. *Soft Matter* **15**, 4818–4826 (2019).
26. Cui, H. *et al.* Spontaneous and X-ray-Triggered Crystallization at Long Range in Self-Assembling Filament Networks. *Science (80-.)*. **327**, 555–560 (2010).
27. Palmer, L. C. *et al.* Long-range ordering of highly charged self-assembled nanofilaments. *J. Am. Chem. Soc.* **136**, 14377–14380 (2014).
28. Gobeaux, F. *et al.* Structural role of counterions adsorbed on self-assembled peptide nanotubes. *J. Am. Chem. Soc.* **134**, 723–733 (2012).
29. Zhang, S. *et al.* A self-assembly pathway to aligned monodomain gels. *Nat. Mater.* **9**, 594–601 (2010).

30. Weingarten, A. S. *et al.* Self-assembling hydrogel scaffolds for photocatalytic hydrogen production. *Nat. Chem.* **6**, 964–970 (2014).
31. Gardel, M. L. *et al.* Elastic behavior of cross-linked and bundled actin networks. *Science (80-.)*. **304**, 1301–1305 (2004).
32. Wong, G. C. L. *et al.* Lamellar Phase of Stacked Two-Dimensional Rafts of Actin Filaments. *Phys. Rev. Lett.* **91**, 1–4 (2003).
33. Pelletier, O. *et al.* Structure of actin cross-linked with [formula presented]-actinin: A network of bundles. *Phys. Rev. Lett.* **91**, 3–6 (2003).
34. Liu, R. *et al.* “Nano-Fishnet” Structure Making Silk Fibers Tougher. *Adv. Funct. Mater.* **26**, 5534–5541 (2016).
35. Kim, U. J. *et al.* Structure and properties of silk hydrogels. *Biomacromolecules* **5**, 786–792 (2004).
36. Fink, T. D. & Zha, R. H. Silk and Silk-Like Supramolecular Materials. *Macromol. Rapid Commun.* **39**, 1–17 (2018).
37. Rathore, O. & Sogah, D. Y. Nanostructure formation through β -sheet self-assembly in silk-based materials. *Macromolecules* **34**, 1477–1486 (2001).
38. Smeenk, J. M. *et al.* Fibril formation by triblock copolymers of silklike β -sheet polypeptides and poly(ethylene glycol). *Macromolecules* **39**, 2989–2997 (2006).
39. SasView. SasView 3.1.2 Documentation. Available at: https://www.sasview.org/docs/old_docs/3.1.2/index.html. (Accessed: 15th November 2022)
40. Baccile, N. *et al.* Self-Assembly Mechanism of pH-Responsive Glycolipids: Micelles, Fibers, Vesicles, and Bilayers. *Langmuir* **32**, 10881–10894 (2016).
41. Qiao, Y. *et al.* Metal-Driven Hierarchical Self-Assembled One-Dimensional Nanohelices. *Nano Lett.* **9**, 4500–4504 (2009).
42. Oda, R., Artzner, F., Laguerre, M. & Huc, I. Molecular structure of self-assembled chiral nanoribbons and nanotubules revealed in the hydrated state. *J. Am. Chem. Soc.* **130**, 14705–14712 (2008).
43. Lis, L. J., Quinn, P. J. & Collins, J. M. Structures and Mechanisms of Phase Transitions in Surfactant Mixtures: Systems Which Induce the Ribbon Phase. *Mol. Cryst. Liq. Cryst. Inc. Nonlinear Opt.* **170**, 119–133 (1989).
44. Hyde, S. T. Identification of Lyotropic Liquid Crystalline Mesophases. in *Handbook of Applied Surface and Colloid Chemistry*. (ed. Holmberg, K.) 299 (John Wiley & Sons, Ltd, 2001). doi:10.1002/asna.18730821002
45. Cuvier, A.-S. S. *et al.* pH-triggered formation of nanoribbons from yeast-derived glycolipid biosurfactants. *Soft Matter* **10**, 3950–3959 (2014).
46. Masuda, M. & Shimizu, T. Lipid nanotubes and microtubes: Experimental evidence for unsymmetrical monolayer membrane formation from unsymmetrical bolaamphiphiles. *Langmuir* **20**, 5969–5977 (2004).
47. Baccile, N. *et al.* Palmitic Acid Sophorolipid Biosurfactant: From Self-Assembled Fibrillar Network (SAFiN) To Hydrogels with Fast Recovery. *Philos. Trans. A* **379**, 20200343 (2021).
48. Greaves, T. L. *et al.* How ionic species structure influences phase structure and transitions from protic ionic liquids to liquid crystals to crystals. *Faraday Discuss.* **206**, 29–48 (2018).
49. Mannock, D. A. *et al.* The thermotropic phase behaviour and phase structure of a homologous series of racemic β -d-galactosyl dialkylglycerols studied by differential scanning calorimetry and X-ray diffraction. *Chem. Phys. Lipids* **148**, 26–50 (2007).